

# Rapid Determination of Oxygen Saturation and Vascularity for Cancer Detection

Fangyao Hu<sup>1\*</sup>, Karthik Vishwanath<sup>1</sup>, Justin Lo<sup>1</sup>, Alaattin Erkanli<sup>2</sup>, Christine Mulvey<sup>1</sup>, Walter T. Lee<sup>3,4</sup>, Nimmi Ramanujam<sup>1</sup>

**1** Department of Biomedical Engineering, Duke University, Durham, North Carolina, United States of America, **2** Department of Biostatistics and Bioinformatics, Duke University, Durham, North Carolina, United States of America, **3** Division of Otolaryngology–Head and Neck Surgery, Duke University Medical Center, Durham, North Carolina, United States of America, **4** Section of Otolaryngology–Head and Neck Surgery, Veterans Administration Medical Center, Durham, North Carolina, United States of America

## Abstract

A rapid heuristic ratiometric analysis for estimating tissue hemoglobin concentration and oxygen saturation from measured tissue diffuse reflectance spectra is presented. The analysis was validated in tissue-mimicking phantoms and applied to clinical measurements in head and neck, cervical and breast tissues. The analysis works in two steps. First, a linear equation that translates the ratio of the diffuse reflectance at 584 nm and 545 nm to estimate the tissue hemoglobin concentration using a Monte Carlo-based lookup table was developed. This equation is independent of tissue scattering and oxygen saturation. Second, the oxygen saturation was estimated using non-linear logistic equations that translate the ratio of the diffuse reflectance spectra at 539 nm to 545 nm into the tissue oxygen saturation. Correlations coefficients of 0.89 (0.86), 0.77 (0.71) and 0.69 (0.43) were obtained for the tissue hemoglobin concentration (oxygen saturation) values extracted using the full spectral Monte Carlo and the ratiometric analysis, for clinical measurements in head and neck, breast and cervical tissues, respectively. The ratiometric analysis was more than 4000 times faster than the inverse Monte Carlo analysis for estimating tissue hemoglobin concentration and oxygen saturation in simulated phantom experiments. In addition, the discriminatory power of the two analyses was similar. These results show the potential of such empirical tools to rapidly estimate tissue hemoglobin in real-time spectral imaging applications.

**Citation:** Hu F, Vishwanath K, Lo J, Erkanli A, Mulvey C, et al. (2013) Rapid Determination of Oxygen Saturation and Vascularity for Cancer Detection. PLoS ONE 8(12): e82977. doi:10.1371/journal.pone.0082977

**Editor:** Jonathan A. Coles, Glasgow University, United Kingdom

**Received:** February 13, 2013; **Accepted:** November 1, 2013; **Published:** December 16, 2013

**Copyright:** © 2013 Hu et al. This is an open-access article distributed under the terms of the Creative Commons Attribution License, which permits unrestricted use, distribution, and reproduction in any medium, provided the original author and source are credited.

**Funding:** This study is supported by National Institutes of Health grant no. 1R01EB011574-01A1, 1R21CA 108490-01A2 and 1R01CA 100559-05 (<http://www.nih.gov/>). The funders had no role in study design, data collection and analysis, decision to publish, or preparation of the manuscript.

**Competing Interests:** The authors have declared that no competing interests exist.

\* E-mail: fangyao.hu@duke.edu

## Introduction

Numerous studies have shown that the early detection and treatment of oral and cervical cancers significantly improve survival rates [1–8]. Detection of precancerous and cancerous oral lesions is mostly accomplished through visual inspection followed by the biopsy of suspicious tissue sites. For cervical cancer screening, the Papanicolaou test or Pap smear is the standard of care. If the Pap smear is positive, colposcopy (visualization of the acetic acid stained cervix with a low power microscope) and biopsy are performed. An effective cancer screening and diagnostic program often requires both sophisticated and expensive medical facilities with well-trained and experienced medical staff. In developing countries, however, there is the absence of appropriate medical infrastructure and resources to support the organized screening and diagnostic programs that are available in the U.S. Therefore, there is a critical global need for a portable, easy-to-use, reliable and low cost device that can rapidly screen for oral and cervical cancer in low-resource settings.

UV-visible (UV-VIS) diffuse reflectance spectroscopy, which can be used to measure tissue absorption and scattering, has shown potential for the early diagnosis of cancers in the cervix and oral cavity [9–24]. The absorption and scattering coefficients of

epithelial tissues reflect the underlying physiological and morphological properties [25]. In the UV-VIS band, the dominant absorbers in oral and cervical tissues are oxygenated and deoxygenated hemoglobin, arising from blood vessels in the stroma. Light scattering is primarily associated with cell nuclei and organelles in the epithelium, as well as collagen fibers and cross-links in the stroma. Neoplastic tissues exhibit significant changes in their physiological and morphological characteristics that can be quantified optically. The contribution of absorption in the stromal layer is expected to increase with neovascularization and angiogenesis, and the oxygen saturation in blood vessels is expected to decrease as the neoplastic tissue outgrows its blood supply. Stromal scattering is expected to decrease with neoplastic progression due to degradation of extracellular collagen networks. [11,25–29]. However, epithelial scattering is expected to increase due to increased nuclear size, increased DNA content, and hyperchromasia [25–27,30]. UV-VIS diffuse reflectance spectroscopy has a penetration depth that can be tuned to be comparable to the thickness of the epithelial layer or deeper to probe both the epithelial and stromal layers [17,25,31].

Our group has developed a UV-VIS diffuse reflectance spectroscopy system with a probe geometry that is most sensitive to changes in the stroma and a scalable inverse Monte Carlo (MC)

reflectance model to rapidly measure and quantify tissue optical properties [32,33]. Chang et al. [10] used the spectroscopic system and the MC model to identify optical biomarkers that vary with different grades of cervical intraepithelial neoplasia (CIN) from normal cervical tissues in 38 patients. Total hemoglobin was found to be statistically higher in high-grade dysplasia compared with normal and low grade dysplasia ( $P < 0.002$ ), whereas scattering was significantly reduced in dysplasia compared with normal tissues ( $P < 0.002$ ). Beumer et al. used the same UV-VIS diffuse reflectance spectroscopy system in an *in vivo* clinical study in which 21 patients with mucosal squamous cell carcinoma of the head and neck were evaluated [34]. All 21 patients underwent panendoscopy and biopsies were taken from the malignant and the contralateral normal tissues. Diffuse reflectance spectra were measured prior to biopsy. The vascular oxygen saturation ( $SO_2$ ) was found to be statistically higher in malignant tissues compared to non-malignant tissues ( $P = 0.001$ ).

The most efficient and effective strategy for the prevention of advanced cervical or oral cancers in resource-limited settings is to see and treat the patient in a single-visit, thus obviating the need for a multi-tiered system such as that in the U.S. where screening, diagnosis, and treatment entail three or more visits to the healthcare facility. For example, guidelines have been written by the Alliance for the Prevention of Cervical Cancer (APCC) on strategies for screening cervical cancer in resource-limited settings [35]. Their recommendation is visual inspection with acetic acid (VIA), followed by treatment of the pre-cancerous lesions using cryotherapy (freezing) [36–38], which can be carried out by physicians, nurses or midwives. An effective screening/diagnostic strategy that can allow for immediate treatment intervention needs to be able to survey the entire region of interest. Further, the detection strategy should be minimally affected by operator bias or subjective interpretation of images collected from the region of interest. Our current system enables quantitative determination of tissue physiological endpoints, but is limited to evaluating localized regions of the tissue. To survey the entire field of view, it is important to scale the single-pixel fiber-based system into an imaging platform and develop algorithms that can quantify these spectral images. However, development of simple imaging systems requires a significant consolidation of the number of wavelengths, so that imaging spectrographs and broad-band thermal sources can be replaced by simple cameras and LEDs.

The goal of this study was to demonstrate a simple ratiometric analysis for the quantitation of tissue  $SO_2$  and total hemoglobin concentration ([THb]) using a small number of wavelengths in the visible spectral range as a strategy for implementation of rapid surveillance of pre-cancers and cancers in a screening population in resource-limited settings. Several previously published studies have utilized simple ratiometric analyses to compute [THb] or  $SO_2$  from reflectance spectra. For example, ratiometric analyses have been developed to extract  $SO_2$  using ratios at two wavelengths, one where the local differences between the extinction coefficients of oxy- and deoxy- hemoglobin are maximal, and one isosbestic wavelength, where the extinction coefficients of oxy- and deoxy- hemoglobin are the same. In one study [39], the ratio of 431/420 nm was computed and used to calculate  $SO_2$ . However, this study did not account for the effects of tissue scattering. Another study [40] used the optical densities at two isosbestic points, 520 and 546 nm, to determine the contribution of scattering and use the optical density at 555 and 546 nm to extract  $SO_2$  through a linear equation. However, this study did not explore the impact of changes in [THb] on the ratios. Our group has previously developed a ratiometric analysis [41] which computes reflectance ratios at the isosbestic wave-

lengths of hemoglobin, and this analysis was able to rapidly calculate [THb] independent of tissue scattering and  $SO_2$ . For this particular ratiometric analysis, the ratio of the intensities at one visible wavelength (452, 500, or 529 nm) to one ultraviolet wavelength (390 nm) from a diffuse reflectance spectrum was used to extract [THb] using a linear analytical equation. However, this analysis would require an ultraviolet source, which is relatively expensive compared to ubiquitous visible wavelength light sources. In this manuscript, we describe a simple and analytical ratiometric analysis to extract both [THb] and  $SO_2$  in the visible wavelength range that addresses the limitations of previous work by our own group and others. It utilizes two or more intensities at different wavelengths from a diffuse reflectance spectrum and calculates appropriate ratios from them. The derived ratios are then converted to [THb] or  $SO_2$  using analytical equations. Our proposed analysis utilizes only three wavelengths (539, 545 and 584 nm), all in the visible part of the spectrum where light emitting diodes (LEDs) are readily available. We also tested our ratiometric analysis with full spectral MC simulations and experimental phantoms to ensure minimal sensitivity to scattering. In addition, our ratiometric analysis also accounts for [THb] when computing  $SO_2$ .

## Methods

Wavelengths were chosen from 500 nm to 600 nm (visible spectrum) in order to leverage relatively low priced light sources such as LEDs. In addition, deoxy- and oxy-hemoglobin have distinct absorption features in the visible spectrum. Five isosbestic wavelengths and five other wavelengths where the difference of extinction coefficients between deoxy- and oxy-hemoglobin are largest were used to calculate [THb] and  $SO_2$ , respectively. Table 1 lists these wavelengths, which provide a total of ten possible combinations (pairs of isosbestic wavelengths), at which ratios were tested for extraction of [THb] and 25 wavelength combinations at which the reflectance ratios were tested (one isosbestic and one maximal-difference wavelength) for extraction of  $SO_2$ .

Figure 1 briefly provides an overview of the ratiometric analysis including the steps involved in the selection of the best ratios for [THb] and  $SO_2$ . Extractions of [THb] and  $SO_2$  were achieved in two steps. First, the reflectance ratio comprised of isosbestic wavelengths was used to extract [THb]. This was achieved by converting the reflectance ratio into [THb] using a linear equation. For each ratio at isosbestic wavelengths, independent sets of the coefficients  $m$  and  $b$  were generated using MC simulations. Next, the reflectance ratio at one isosbestic wavelength and one maximal-difference wavelength was converted into an  $SO_2$  value using a non-linear equation using the  $\alpha$  (THb) and  $\beta$  (THb) coefficients. These coefficients were generated using MC simulations for each of the 25-reflectance ratios at every simulated [THb]. The extracted [THb] from the first step was used to select the appropriate non-linear logistic equation to convert the ratio of the isosbestic to maximum difference wavelength into the  $SO_2$  value. After the equations for [THb] and  $SO_2$  were developed, the ratiometric analysis was validated with experimental tissue mimicking phantoms. To show the clinical utility of this analysis and its independence to changes in instrumentation, the extractions using the selected ratios were then compared with those using the full spectral MC analysis in three different clinical studies carried out with different optical systems.

**Table 1.** Wavelengths used for extraction of [THb] and SO<sub>2</sub>.

Isosbestic Wavelengths for [THb] (nm)	Wavelengths for Oxygen Saturation (SO <sub>2</sub> ) (nm)
500	516
529	539
545	560
570	577
584	593

doi:10.1371/journal.pone.0082977.t001

**Generating analytical lookup tables for [THb] and SO<sub>2</sub> from reflectance ratios**

Analytical equations to convert appropriate ratios into [THb] and SO<sub>2</sub> values were determined using full spectral MC simulations. The forward full spectral MC model [42] was used to generate 24805 unique diffuse reflectance spectra. These reflectance spectra served as the simulated master set. Diffuse reflectance spectra were simulated by calculating the absorption and scattering spectrum between 350–600 nm. The absorption coefficients were calculated with the assumption that oxy- and deoxy-hemoglobin are the dominant absorbers in tissue. The sum of these two absorber concentrations gave the resulting [THb], which was varied between 5 and 50 μM in increments of 0.1 μM in the master set. The concentration of each hemoglobin species was varied to span the range of SO<sub>2</sub> values from 0 to 1, in steps of 0.1. The reduced scattering coefficients, μ<sub>s</sub>’, across the spectral range were determined using Mie theory for 1 μm polystyrene microspheres. Five different scattering levels were generated by increasing the number density of sphere concentrations. The wavelength-averaged (between 350–600 nm) mean reduced scattering coefficients for these five scattering levels were 8.9,

13.3, 17.8, 22.2, and 26.6 cm<sup>-1</sup>. The resulting master set consisted of 24805 reflectance spectra, which represent the combination of all possible [THb] levels, with all SO<sub>2</sub> levels, and all scattering levels (451×11×5 = 24805). These optical properties are similar to those used in our previous study [41]. The simulated reflectance spectra for the master set were created for a fixed fiber-probe geometry, as described previously [42]. Finally, an experimentally measured diffuse reflectance spectrum with the same fiber-geometry was used as a “reference” to calibrate the scale of the simulated spectra to be comparable to that of measured spectra.

To study the impact on extraction accuracy of the ratiometric analysis with increasing spectral bandpasses, we simulated additional bandpasses in the master set. The reflectance spectra were simulated for three different bandpasses (2 nm, 3.5 nm and 10 nm full width-half-maximum (FWHM) bandwidths) and resulted in 3 modified master diffuse reflectance sets (each containing 24,805 spectra). This was done by assuming each wavelength had a certain Gaussian bandpass of specified FWHM. Specifically, the reflectance at each wavelength in the simulated spectrum was convolved with a Gaussian distribution function with the specific bandpass. Equations to convert reflectance ratios into [THb] and SO<sub>2</sub> were then generated separately for each of the three bandpass-modified master diffuse reflectance spectral sets.

Figure 2 describes the development of analytical equations used to compute [THb] and SO<sub>2</sub>. A [THb] ratio, 584/545, and an SO<sub>2</sub> ratio, 539/545, are shown as examples. For [THb] extraction, the reflectance ratio at a given wavelength-pair was computed from every simulated reflectance spectrum that had a fixed [THb]. Thus, there were 55 values for a given [THb] wavelength-ratio (across the 5 scattering levels and 11 SO<sub>2</sub> levels). Eleven of these values were averaged across SO<sub>2</sub>, for each scattering level. For each of the ten isosbestic wavelength-pairs, the dependence of the reflectance ratio on [THb] was plotted across all SO<sub>2</sub> levels and

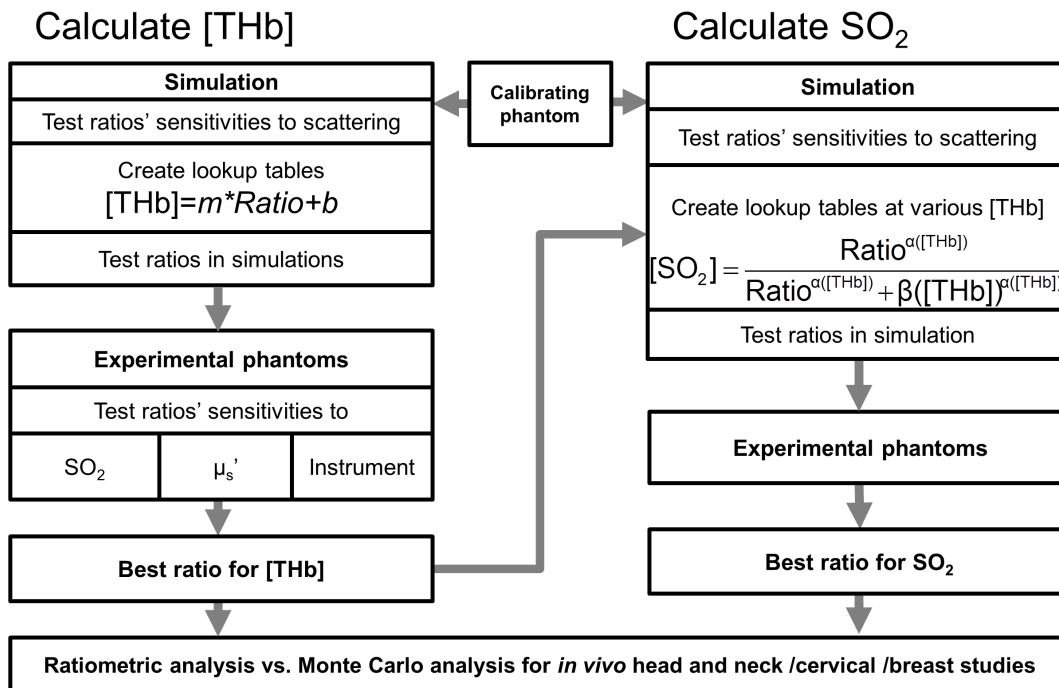


**Figure 1.** Flow chart illustrating the ratiometric analysis for [THb] and SO<sub>2</sub> estimation.

doi:10.1371/journal.pone.0082977.g001

each scattering level, as shown in Figure 2A. Although the analysis consisted of 5–50  $\mu\text{M}$  [THb] in steps of 0.1  $\mu\text{M}$ , only 10 of the 451 [THb] levels are shown in the figure for easier interpretation of the data points. We evaluated the dependence of the reflectance ratio for a given wavelength-pair on tissue  $\text{SO}_2$  and scattering. The horizontal error bars at each scattering level show the spread of the reflectance ratio due to varying  $\text{SO}_2$  levels from 0 to 1. This reflects the sensitivity of the ratio to changes in  $\text{SO}_2$ . The spread in the different symbols at each [THb] reflects the sensitivity of the ratio to scattering. The reflectance ratios at each [THb] were averaged across the 5 scattering levels and the 11  $\text{SO}_2$  levels, and a linear analytical equation was generated for the averaged ratios. Figure 2B shows the linear analytical equations for 584/545, 584/570, 570/545, and 584/529 as examples.

In order to convert the reflectance ratio computed at a given  $\text{SO}_2$  wavelength-pair into an  $\text{SO}_2$  value, a non-linear logistic (Hill curve) equation was used. A unique Hill equation was generated for each of the 451 [THb] (5–50  $\mu\text{M}$  in 0.1 increment steps) in the modified master set. The reflectance ratio for a given  $\text{SO}_2$  wavelength-pair, at a given [THb], was averaged across the five scattering levels (Figure 2C). This resulted in 11 averaged ratios for each  $\text{SO}_2$  wavelength pair, at each [THb]. The Hill coefficients were generated by fitting the 11 averaged ratios to the logistic equation. Since a total of 451 different [THb] values were used in the simulations, 451 different equations were generated for each  $\text{SO}_2$  wavelength-pair. Figure 2D shows the example figures of the Hill curves generated from the averaged ratios at different [THb] for 539/545.

### Determination of the best ratios from simulation and experimental phantoms

A total of 8 sets of reflectance spectra were used to validate the ratiometric analysis. The optical properties and collection parameters for these 8 phantom sets are summarized in Table 2. Phantom sets 1–3 were simulated with the scalable MC model, as described above. Phantom sets 4–8 were experimentally measured data and have been described in detail previously [41,43]. Briefly, Phantom Set 4 consisted of 51 phantoms with varying  $\text{SO}_2$  levels but with a fixed [THb] (14.8  $\mu\text{M}$ ), and  $\mu_s'$  level (12.6  $\text{cm}^{-1}$ ). Phantom Set 5 consisted of two subsets of phantoms with a low scattering level ( $\mu_s' = 13.5 \text{ cm}^{-1}$ ) and high scattering level ( $\mu_s' = 22.52 \text{ cm}^{-1}$ ). Each set in Phantom Set 5 consisted of 4 phantoms. Each phantom in the low scattering level was paired with a phantom in the high scattering level and the [THb] value of each paired phantom was the same. The standard deviation of the reflectance for each wavelength-pair in each paired phantoms were computed. Phantom Set 6 consisted of 13 phantoms with increasing [THb] from 5.86–35.15  $\mu\text{M}$ . The averaged  $\mu_s'$  levels decreased for each phantom from 23.63 to 17.30  $\text{cm}^{-1}$ . A second instrument was used to measure the phantoms for Phantom Set 7 and Set 8 to validate the instrument independence of the ratiometric analysis. Phantom Set 7 was similar to Phantom Set 5 in that it contained two sets of 4 phantoms with low and high scattering levels ( $\mu_s' = 13.5 \text{ cm}^{-1}$  and 22.89  $\text{cm}^{-1}$  respectively) and paired phantoms from each level contained the same [THb]. The standard deviation of the reflectance for each wavelength-pair in each paired phantoms were also computed. Phantom Set 8 consisted of 16 phantoms with increasing [THb] from 5–50  $\mu\text{M}$ . The  $\mu_s'$  level of each phantom was lower than the previous phantom, ranging from 28.56 to 17.02  $\text{cm}^{-1}$ , due to serial dilutions of the phantom solution. The combination of all of these experimental tissue phantoms measured serves to determine the best ratios to estimate [THb] and  $\text{SO}_2$  for a wide range of optical properties measured by different instruments.

The ratiometric analysis was first tested on the simulated reflectance. Linear analytical equations for [THb] ratios and the non-linear logistic equations for  $\text{SO}_2$  ratios were generated from Phantom Sets 1–3. The extracted values of [THb] using the ratiometric analysis were compared to the true values for each diffuse reflectance spectrum and the absolute errors between the predicted and true values were calculated. Next, the sensitivity of each [THb] ratio to scattering was computed using the standard deviation of the reflectance ratio at each [THb].

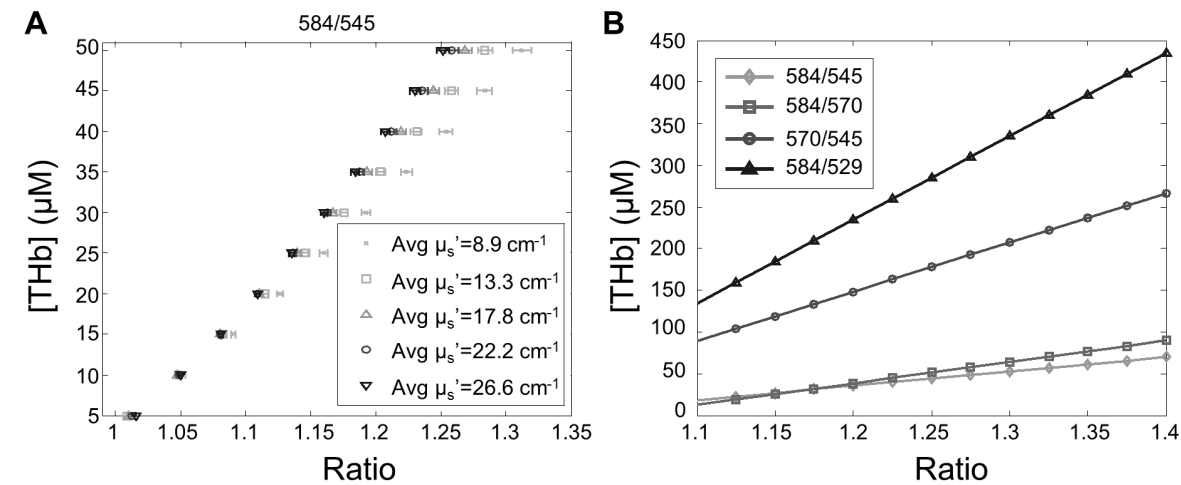
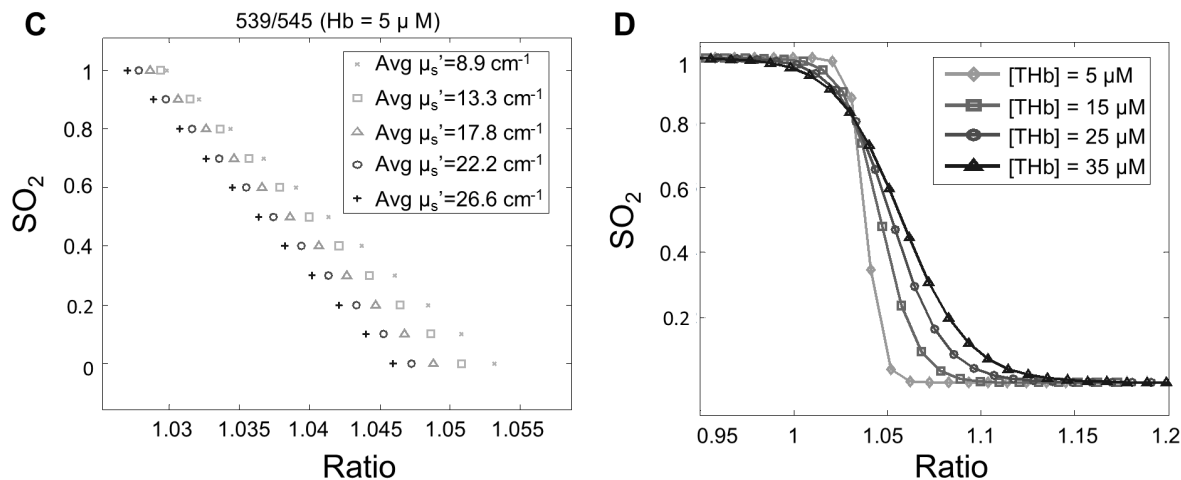
The calculation of [THb] using the ratiometric analysis was also validated in Phantom Sets 4–8. Since every reflectance spectrum simulated by the MC model needs to be scaled by a calibrating phantom, the choice of the calibrating phantom can introduce systematic errors. To account for these effects on the extracted [THb], 3 different phantoms in Phantom Set 4, Set 6 and Set 8 and 2 different phantoms in Sets 5 and 7 were selected as the calibrating phantoms. The  $\text{SO}_2$ , [THb] and  $\mu_s'$  of the calibrating phantoms are summarized in Table 2. Each time a calibrating phantom was selected, a new master set of reflectance was generated with the scalable MC model, and new coefficients for analytical equations were generated from these phantom sets. The generated analytical equations were used to extract the [THb] or  $\text{SO}_2$  values in the same experimental phantom sets from which the calibrating phantoms were selected. This ensured that the systematic errors or titration errors in one experimental phantom study were restricted to the same experimental phantom study and were not carried to another experimental phantom study. The probe geometries and bandpasses for the simulated master sets were matched to the experimental system. The ratiometrically extracted [THb] were compared to the MC extracted [THb] of the experimental phantoms for each phantom in Sets 4–8 to compute the absolute errors. The ratio spreads of the ten possible isosbestic wavelength pairs were computed from the paired phantoms in Set 5 and Set 7. The best ratio for [THb] was determined from the error and ratio spread rankings both with the simulated data and with the experimental data.

The ratiometric analysis for  $\text{SO}_2$  was validated in Phantom Set 4, which consisted of phantoms with varying  $\text{SO}_2$  levels. For each experimental phantom in this set, [THb] was first computed using the best isosbestic wavelength-pair using the ratiometric analysis. This extracted [THb] was then used to select the corresponding Hill curve coefficients for a given  $\text{SO}_2$  wavelength-pair. The reflectance ratio of each  $\text{SO}_2$  wavelength-pair was first computed and then converted to a  $\text{SO}_2$  value with the corresponding Hill curve coefficients. The ratiometrically extracted  $\text{SO}_2$  values were compared against the  $\text{SO}_2$  values measured with a  $\text{pO}_2$  electrode, as previously described [43]. To evaluate the sensitivity of each  $\text{SO}_2$  ratio to scattering, the reflectance ratios of each  $\text{SO}_2$  wavelength-pair were first computed in every phantom of Phantom Sets 5 and Set 7. The standard deviations were then computed from each paired reflectance ratios for each  $\text{SO}_2$  wavelength-pair since only the scattering was different within each paired phantom. The derived standard deviations from every paired phantom in Phantom Set 5 and Set 7 were averaged for each  $\text{SO}_2$  wavelength-pair.

### Instrumentation used in phantoms and clinical studies

Three instruments were used to validate the ratiometric analysis in this manuscript. Instrument A was used in the experimental phantom studies (Set 4–6) and in an *in vivo* cervical study [41,43] [44]. Instrument B was also used in the experimental phantom studies (Set 7–8), and also in the *in vivo* cervical study [44] and in an *in vivo* breast cancer study [45]. Instrument C was used for an *in vivo* head and neck cancer study. The details of Instrument A, B

## Analytical equation for [THb] estimation

Analytical equation for  $\text{SO}_2$  estimation

**Figure 2. Steps for calculating the analytical equations.** Steps for calculating the analytical equations: (A) Generating reflectance with various optical properties using forward analysis and derived Hb ratios. The horizontal error bars show the standard deviation of the ratios at  $\text{SO}_2$  levels from 0 to 1. The spreads are small because the ratios are derived from isosbestic points. (B) Example linear analytical equations of 584/545, 584/570, 570/545, and 584/529 for [THb] estimation. (C) Calculating  $\text{SO}_2$  ratios with several scattering levels at one [THb] (D) Hill curve equations were generated at several [THb] for each  $\text{SO}_2$  ratio. Only 539/545 is shown. doi:10.1371/journal.pone.0082977.g002

and C and the probe geometries have been previously described [44–47]. Briefly, Instrument A consisted of a 450 W xenon (Xe) arc lamp (JY Horiba, Edison NJ), double-excitation monochromators (Gemini 180, JY Horiba, Edison, NJ), and a Peltier-cooled open-electrode charge-coupled device (CCD) (Symphony, JY Horiba, Edison, NJ) [45] [43] [44]. Instrument B was a fiber-coupled spectrophotometer (SkinScan, JY Horiba, Edison, NJ), which consisted of a 150 W Xe arc lamp, a double-grating excitation monochromator, an emission monochromator, and an extended red photomultiplier tube (PMT) [44] [43]. Instrument C was a portable system, which consisted of a 20 W halogen lamp (HL2000HP; Ocean Optics, Dunedin, FL), heat filter (KG3, Schott, Duryea, PA), and an USB spectrometer (USB4000, Ocean Optics, Dunedin, FL) [47]. Illumination and collection for all instruments were achieved by coupling to fiber optic probes. The instrument parameters are listed in Figure 3.

## Testing the ratiometric analysis with various scattering powers

The power law ( $\mu_s' = a \cdot \lambda^{-b}$ ) was used to model the reduced scattering coefficients where  $a$  determines the overall magnitude of scattering,  $\lambda$  is wavelength, and  $b$  is the scattering power. A new set of 1500 reflectance spectra (10 [THb] levels, 5  $\text{SO}_2$  levels, and 10 different scattering powers with the scattering values equal to 2, 6, or  $10 \text{ cm}^{-1}$  at 600 nm) were simulated with the forward Monte Carlo model using the scattering coefficient generated from the power law. The scattering power was varied from 0.2 to 2 with steps of 0.2. The [THb] were range from 5 to 50  $\mu\text{M}$  in steps of 5. The  $\text{SO}_2$  levels were range from 0 to 1 with increment of 0.25. Table 3 summarizes the optical properties used for testing the ratiometric analysis with various scattering powers. The [THb] and the  $\text{SO}_2$  were extracted with the ratiometric analysis for the best ratios determined in Section 3.1. The absolute [THb] and  $\text{SO}_2$  errors were computed. In addition, the scattering powers of

**Table 2.** Optical properties for simulated and experimental tissue-mimicking phantoms.

Set	Type	Instrument	Bandpass (nm)	SO <sub>2</sub>	[THb] (μM)	<μ <sub>s</sub> '> (cm <sup>-1</sup> )
1	Simulation	-	2	0–1	5–50	8.9–26.6
2	Simulation	-	5	0–1	5–50	8.9–26.6
3	Simulation	-	10	0–1	5–50	8.9–26.6
4	Experiment	A	2	0–1	14.8	12.6
5	Experiment	A	2	1	6.4–14.3	13–21.7
6	Experiment	A	2	1	5.9–35.2	17.3–23.6
7	Experiment	B	3.5	1	7.3–16.2	14.3–21.9
8	Experiment	B	3.5	1	5.0–50.0	13.0–21.9

doi:10.1371/journal.pone.0082977.t002

the clinical data in this manuscript were computed by fitting the Monte Carlo-extracted wavelength-dependent scattering coefficients to the scatter power model.

### Comparison of the speed of the MC and ratiometric analyses

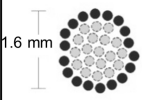
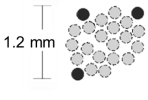
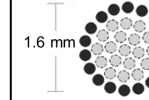
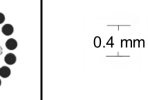
To compare the computational performance of the ratiometric analysis and the full spectral MC analysis for extraction of [THb] and SO<sub>2</sub>, 100 diffuse reflectance spectra with randomly selected [THb] and SO<sub>2</sub> values were simulated with the forward MC model. Random white noise was also added to each simulated reflectance spectrum before the fitting process. The amplitude of the generated random noise was limited to two percent of the difference between the simulated maximum and the minimum values of each reflectance spectrum. The noise level was determined from our previous study in which the worst SNR of instrument A is 44.58 dB. This means the amplitude of the noise is about two percent of the amplitude of the signal. These spectra were then analyzed using both the inverse full spectral MC analysis and the ratiometric analysis. The ratiometric analyses on these samples used the best ratios, which are described in the subsequent sections of this manuscript, for [THb] and SO<sub>2</sub>. The extracted [THb] and SO<sub>2</sub> values for the full spectral MC analysis and the ratiometric analysis were compared to the expected (input)

values and absolute errors were computed. The data processing time for both analyses were also compared.

### Clinical validation

To test the robustness of the ratiometric analysis in *in vivo* clinical settings, we applied the ratiometric analysis in three separate studies conducted on three different tissue sites. These clinical studies used diffuse reflectance spectroscopy to differentiate normal versus malignant or precancerous tissues *in vivo* in the cervix [44], in the breast [45], and in the head and neck [34]. The samples from these studies represent different optical absorption scenarios. Head and neck [34] and breast tissues have relatively high [THb] while the cervix has [THb] values at the lower end of the spectrum [44]. The ranges of [THb] from our previous results were 2.6–208.9 μM, 0.79–63.7 μM and 0.99–44.06 μM, for the head and neck, breast, and cervical tissues, respectively. In addition, breast tissue contains not only [THb] but also β-carotene as an additional absorber [45]. Data previously collected for the clinical studies and analyzed with the scalable full spectral MC analysis were used to evaluate the ratiometric analysis. The study designs and the protocols of these *in vivo* studies are described previously [44,45]. All clinical studies in this manuscript were reviewed and approved by the Duke University School of Medicine Institutional Review Board. Written informed consents were obtained from each patient in these *in vivo* studies. The averaged diffuse reflectance spectrum for each site from each study was analyzed with both the inverse full spectral MC analysis and the ratiometric analysis. Pearson correlation coefficients between the full spectral MC and ratiometric analysis extracted [THb] and SO<sub>2</sub> values were calculated for each clinical study.

In the cervical study, patients referred from the Duke University Medical Center (DUMC) Colposcopy Clinic after abnormal Papanicolaou tests were recruited. A fiber optic probe was used to deliver and collect the diffuse reflectance (350–600 nm) from one to three visually abnormal sites immediately after colposcopic examination of the cervix with the application of 5% acetic acid. This was followed by an optical measurement on a colposcopically normal site from the same patient. Optical measurements of colposcopically normal and abnormal sites were taken prior to biopsy to avoid confounding absorption due to superficial bleeding. Diffuse reflectance from 76 sites in 38 patients were normalized by a reflectance standard and interpolated prior to calculating the reflectance ratios. Reduced scattering coefficients,

		Instrument A		Instrument B	Instrument C
Illumination	Setting	0-order		Synchronous with detection	20 W Halogen light source with a short-pass heat protection filter
Collection	Bandpass (Slit width)	1.9 nm(0.6 mm)		3.5 nm(0.5 mm)	1.5 nm (0.2 mm)
	Sampling Increment	0.13 or 0.26 nm		5 nm	0.22 nm
	Spectral range	350–600 nm		350–600 nm	400–800 nm
Probe geometry					
Illumination fiber	Phantom & cervix study	Breast study	Phantom & cervix study	Head and neck study	
Collection fiber					

**Figure 3.** Illumination and collection parameters of the instruments used in experimental phantoms and clinical studies.

doi:10.1371/journal.pone.0082977.g003

**Table 3.** Optical properties used for testing the ratiometric analysis with various scattering powers.

[THb] ( $\mu\text{M}$ )	$\text{SO}_2$	Scattering Power	Avg. $\mu_s'$ (350~600 nm)		
			$\mu_s' = 2 \text{ (cm}^{-1}\text{) at 600 nm}$	$\mu_s' = 6 \text{ (cm}^{-1}\text{) at 600 nm}$	$\mu_s' = 10 \text{ (cm}^{-1}\text{) at 600 nm}$
5-50	0-1	0.2	2.05	6.17	10.28
5-50	0-1	0.4	2.11	6.34	10.57
5-50	0-1	0.6	2.17	6.52	10.87
5-50	0-1	0.8	2.24	6.71	11.18
5-50	0-1	1	2.30	6.91	11.51
5-50	0-1	1.2	2.37	7.11	11.84
5-50	0-1	1.4	2.43	7.32	12.20
5-50	0-1	1.6	2.51	7.54	12.56
5-50	0-1	1.8	2.59	7.77	12.94
5-50	0-1	2	2.67	8.00	13.34

doi:10.1371/journal.pone.0082977.t003

[THb] and  $\text{SO}_2$  were also extracted from the same data using the inverse full spectral MC analysis [42].

For the head and neck cancer *in vivo* study, 42 enrolled patients had undergone panendoscopy with biopsy at Durham Veterans Administration Medical Center or DUMC. After the consented patient was under general anesthesia, the optical probe was placed on at least two sites: a clinically suspicious site and a distant normal site with normal mucosa appearance whose location was contralaterally matched to the suspicious site. At least 5 diffuse reflectance spectra were measured for each site. The biopsies were obtained immediately after the probe was removed from the measured clinical suspicious sites. All measurements were calibrated to the reflectance standard measured on the day of the surgery. In this head and neck study, the utility of the physiological and morphological endpoints obtained via the quantitative diffuse reflectance spectroscopy technique was investigated for the classification of head and neck squamous cell carcinoma at the time of staging panendoscopy. Malignant and non-malignant tissues were initially stratified by diagnosis and further classified by anatomical and morphological groupings to determine the most effective approach to discriminate squamous cell carcinoma (SCC) from its benign counterparts.

In the breast cancer study, thirty-five patients undergoing either a modified radical mastectomy or partial mastectomy for invasive and noninvasive breast malignancies were recruited at DUMC. The surgeon first located the lesion under ultrasound guidance; then, either a 10-gauge or 14-gauge biopsy needle coaxial cannula was guided through a small incision in the skin into the region of interest. A diffuse reflectance measurement (350–600 nm) was collected at a distance of 2 mm past the cannula with a fiber-optic probe after the removal of the needle and residual blood in the field. The optical probe was then retracted, and a biopsy needle was inserted through the cannula and a biopsy sample was removed. This resulted in the removal of a typically 20-mm-long cylinder of tissue, the proximal end of which corresponded to the volume optically measured by the probe. Tissue reflectance spectra from biopsies were normalized by the diffuse reflectance measured from an integrating sphere (Labsphere, Inc. North Sutton, NH) at the same day of the surgery for each patient. Biopsy samples were further processed through standard histologic procedures for pathological information.

### Comparing the classification performances of the full spectral MC and the ratiometric analyses

To compare the classification performances of the full spectral MC and ratiometric analyses, we compared the area under the receiver operating curves (AUC) calculated from the logistic regression models built based on the optical biomarkers extracted from the two analyses. We believe the AUC is more representative for the classification performance since the AUC is generated from various cut-off criteria. Since the full spectral MC model is able to extract optical biomarkers rather than just [THb] and  $\text{SO}_2$ , we also included  $\mu_s'$  extracted with the for the full spectral MC model to build the logistic regression model for the cervix, breast and the head and neck groups. Beta-carotene concentrations extracted with the full spectral MC model were also included to build the logistic regression model for the breast group. The extracted [THb],  $\mu_s'$  and the beta-carotene concentrations were log transformed before building the logistic regression model. The  $p$  values were computed based on the method published by DeLong et al [48]. for comparing the ROC curves. All logistic regression models and the  $p$  values are computed with the SAS software (SAS Institute Inc., Cary, NC, USA)..

## Results

### The best ratio for estimating [THb] and $\text{SO}_2$ from simulated and experimental phantoms

The accuracy of the 10 isosbestic wavelength-pairs to extract [THb] was evaluated in both simulated and experimental phantoms. Errors in extracted [THb] for each ratio were calculated. Next, the standard deviation of each ratio for changes in tissue scattering and  $\text{SO}_2$  was computed using only the simulated data. The 10 ratios were then ranked using both the standard deviations and the errors. The best ratio should be able to accurately extract [THb] with low sensitivity to both tissue scattering and  $\text{SO}_2$ . A total of 25 wavelength-pairs were available for the calculation of  $\text{SO}_2$ . The accuracy of these wavelength-pairs to determine  $\text{SO}_2$  was also ranked using an identical metric as was used for [THb]. Again, the best ratio should be able to accurately extract  $\text{SO}_2$  with low sensitivity to tissue scattering. Figures 4A and 4B show 6 ratios with the lowest errors to extract [THb] in the simulated and experimental datasets, respectively. Figures 4C and 4D shows the standard deviation of the [THb] ratios for various  $\text{SO}_2$  and scattering levels in the simulated and experimental data,

respectively. Figures 4E-4H show similar data for SO<sub>2</sub>. For [THb] ratios, 584/545 has the lowest average errors for each band pass in both simulated and experimental phantoms. The standard deviation of 584/545 was the third lowest for each band pass in simulated data and the second lowest for each band pass in experimental phantoms. This means that 584/545 can extract [THb] with relatively small errors, and it is relatively insensitive to the scattering or SO<sub>2</sub>. The average errors are comparable in both simulations and in experimental phantoms for the top 6 SO<sub>2</sub> ratios with the exception of 516/500, which has higher errors in the experimental phantom. 539/545 has the lowest average ratio and standard deviation in both simulation and experimental phantoms. Thus, 584/545 and 539/545 were chosen as [THb] and SO<sub>2</sub> ratios for further testing.

### Testing the ratiometric analysis with varying scattering powers

Figure 5 shows the absolute errors of the extracted [THb] and SO<sub>2</sub> for the best [THb] and SO<sub>2</sub> ratios when using the scatter power model. The accuracies for extracting [THb] and SO<sub>2</sub> varied with scattering power. In our data, the average and the standard deviation of the scattering power for head and neck, cervix and breast tissues are  $0.62 \pm 0.12$ ,  $0.55 \pm 0.27$  and  $0.50 \pm 0.16$  respectively.

### Comparison of the speed of the MC and the ratiometric analyses

Figures 6A–C show the comparison of the computational time, the mean error in [THb] extraction, and the mean error in SO<sub>2</sub> extraction using the scalable full spectral MC analysis and the ratiometric analysis. These data were generated using 100 simulated diffuse reflectance spectra. [THb] was extracted using the ratiometric analysis with the ratio computed between 584 nm and 545 nm. The extracted [THb] value from the ratiometric analysis was then used to determine the look-up coefficients to calculate the SO<sub>2</sub> using the 539 nm/545 nm ratio. As shown in Figure 6A, the ratiometric analysis is over 4000 times more computationally efficient compared to the full spectral MC analysis [42]. Figures 6B and 6C show the mean error for [THb] extraction and SO<sub>2</sub> extraction using the full spectral MC analysis and the ratiometric analysis. The mean errors were 0.24 μM and 3.94 μM for [THb] extraction, while the errors were 0.004 and 0.23 for SO<sub>2</sub> values for the MC analysis and the ratiometric analysis, respectively.

### Comparison of MC and ratiometric analysis

Correlation coefficients were computed between the optical endpoints extracted using both analyses for each tissue group in each of the three clinical studies. Table 4 summarizes the Pearson correlation coefficients between the full spectral MC analysis and the ratiometric analysis for [THb] and SO<sub>2</sub> of each tissue group in the cervical pre-cancer, head and neck squamous cell carcinoma, and breast cancer studies. The normal samples in the breast cancer study were further classified into the benign and adipose group, depending on the adipose percentage of the normal sample [45]. The overall correlation coefficient for each study was also computed when all samples in each study were used.

### Accuracy of algorithm in cervical tissues with low tissue vascularity

[THb] was extracted using the inverse full spectral MC analysis from a total of 76 samples from 38 patients, as published previously. The samples were classified as normal, low-grade

cervical intraepithelial neoplasia (CIN 1) and high-grade cervical intraepithelial neoplasia (CIN 2+). Figure 7A shows boxplots for the full spectral MC extracted [THb] for the three tissue groups. Figure 7B shows boxplots for [THb] extracted using the ratiometric analysis for the three tissue groups. To compare with the previously published results extracted by the full spectral MC analysis, a log transformation was applied to the ratiometrically-extracted [THb]. [THb] determined using both analyses was statistically higher in CIN2+ tissues ( $p < 0.01$ ) compared to normal and CIN1 samples. No statistical differences were found when comparing the SO<sub>2</sub> of different tissue groups with the full spectral MC analysis or the ratiometric analysis. The  $p$ -values were derived from the unpaired two-sided student  $t$ -tests for consistency with the previously published data [44].

### Accuracy of algorithm in head and neck tissues with high vascularity

Figure 8 shows boxplots for SO<sub>2</sub> values extracted with full spectral MC analysis and the ratiometric analysis, across all measured tumor and normal sites in head and neck squamous cell carcinoma patients. The samples were separated into 3 groups (glottic, lymphoid and mucosal) based on morphological location of each measurement site. Wilcoxon rank-sum tests were used to establish differences between the extracted SO<sub>2</sub> values in the normal and SCC sites, for each tissue group. The extracted SO<sub>2</sub> was significantly different between SCC and normal samples for the glottic, lymphoid and mucosal tissue groups when extracted using both the full spectral MC analysis ( $p = 0.03$ ,  $p < 0.01$  and  $p = 0.01$  respectively) and the ratiometric analysis. SO<sub>2</sub> values extracted using the ratiometric analysis ( $p < 0.01$  for the 3 groups) showed similar differences between the SCC and normal samples for these tissue groups.

### Accuracy of algorithm in breast tissues with multiple absorbers

Figure 9 shows a boxplot for the inverse full spectral MC or the ratiometrically extracted SO<sub>2</sub> of malignant and normal breast tissues. The normal samples were reclassified into a benign group if the fat content of the tissue biopsy was less than 50% or into the adipose group if the fat content in the biopsy was greater than 50% as described previously [45]. Figure 9A shows boxplots for the full spectral MC extracted SO<sub>2</sub> of the tumor and benign tissues whereas Figure 9B shows boxplots for the ratiometrically extracted SO<sub>2</sub> of tumor and benign tissue from the *in vivo* breast study. Figures 9C and 9D also show boxplots for the SO<sub>2</sub> of the tumor and adipose tissues extracted with both analyses. Wilcoxon rank-sum tests were performed to test the statistical significance of the extracted SO<sub>2</sub> between the tumor samples and normal (both benign and adipose) tissues for both full spectral MC analysis and ratiometric analysis. The extracted SO<sub>2</sub> of the normal samples were significantly higher than the tumor samples ( $p < 0.01$ ) for both the ratiometric analysis and the full spectral MC analysis.

### Comparison the classification performances of the full spectral MC and the ratiometric analyses

The combinations of the optical biomarkers used for building the logistic regression models and the area under the receiver operating curve (ROC) are summarized in Table 5. No significant  $p$  values were observed when comparing the AUC calculated between the two analyses. Representative ROC curves built based on the optical biomarkers extracted from the lymphoid tissues using the full spectral MC and the ratiometric analyses are also shown in Figure 10. The full spectral MC ROC curve in

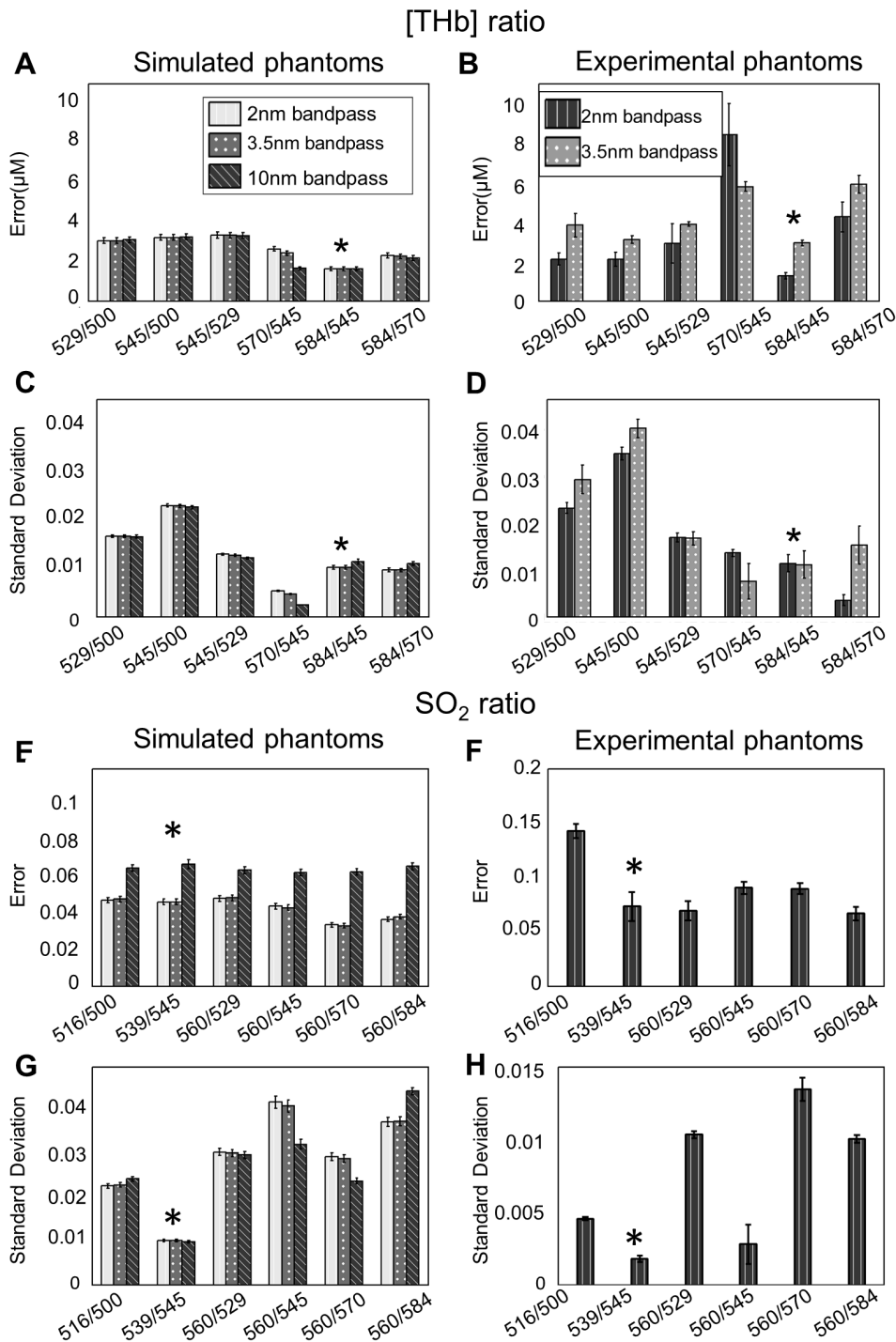


**Figure 4. Results for the simulated phantoms and the experimental phantoms.** Errors and ratio standard deviation of [THb] ratios and SO<sub>2</sub> ratios from simulated phantoms and experimental phantoms. The top 6 ratios as defined by the lowest errors are shown. (A–B) Errors of the top 6 [THb] ratios in simulated data and experimental data. 584/545 has the lowest errors in both simulated phantom data and experimental phantom data. (C–D) Standard deviations of the top 6 [THb] ratios in the simulated data and the experimental data. 570/545, 584/545, and 584/570 have low standard deviation in both data sets. (E–F) Errors of the top 6 SO<sub>2</sub> ratios in the simulated and experimental data. The errors are comparable for these ratios except for 516/500, which has higher errors in the experimental data. (G–H) Standard deviations of the top 6 SO<sub>2</sub> ratios in the simulated data and the experimental data. 539/545 has the lowest standard deviation in both data sets. The best ratios for extracting [THb] or SO<sub>2</sub> are marked with asterisk (\*).

doi:10.1371/journal.pone.0082977.g004

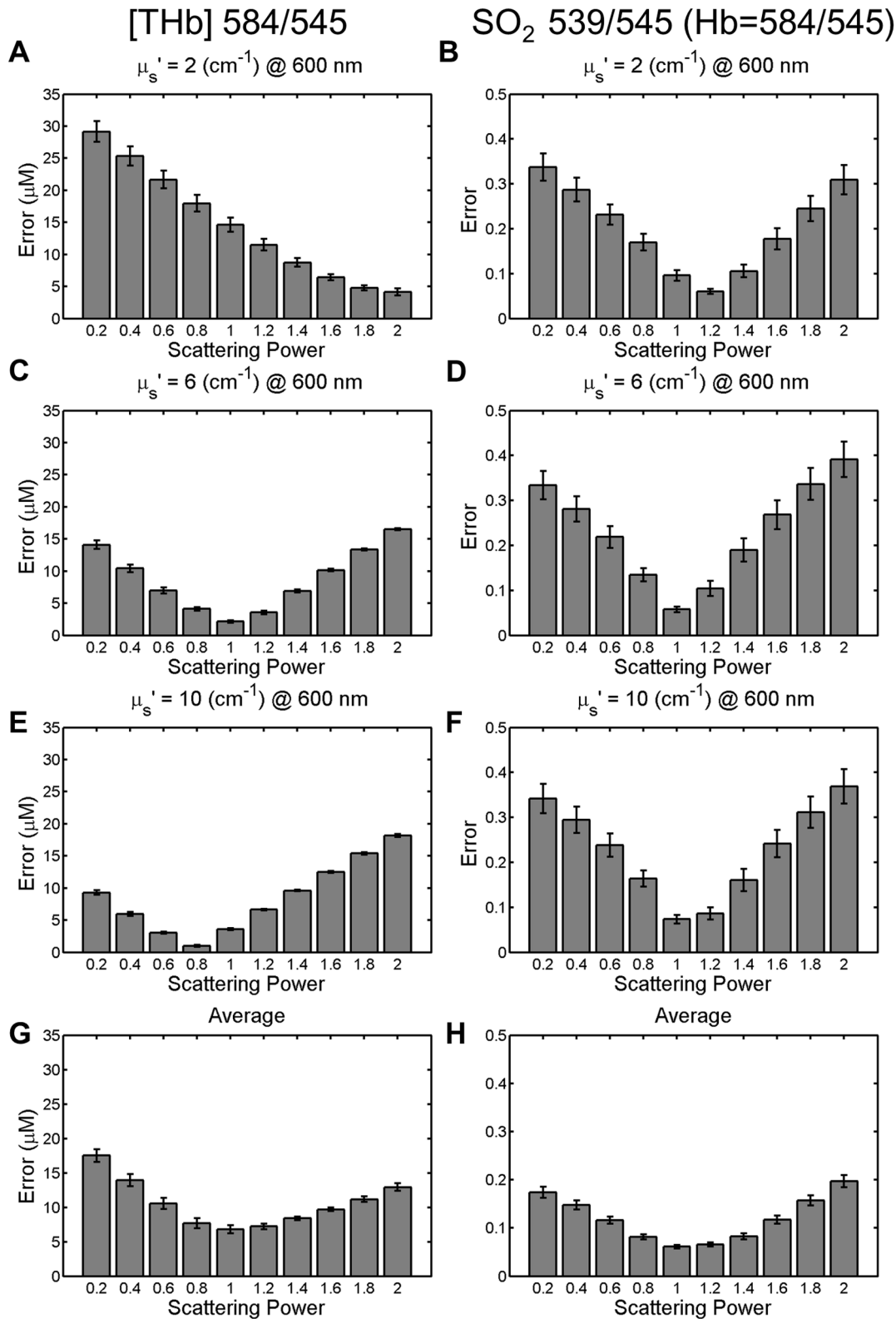


**Figure 5. Average absolute error for best [THb] and SO<sub>2</sub> ratios tested with various scattering powers.** (A), (C), (E) Absolute errors for extracting the [THb] of the simulated reflectance spectra with 584/545 when the scattering power varied from 0.2 to 2 for different scattering levels. (B), (D), (F) Absolute errors for extracting the SO<sub>2</sub> of the simulated reflectance spectra with 539/545 when the scattering power varied from 0.2 to 2 for different scattering levels. (G) Averaged errors from (A), (C) and (E). (H) Average errors from (B), (D) and (F). Error bars represent the standard errors. doi:10.1371/journal.pone.0082977.g005

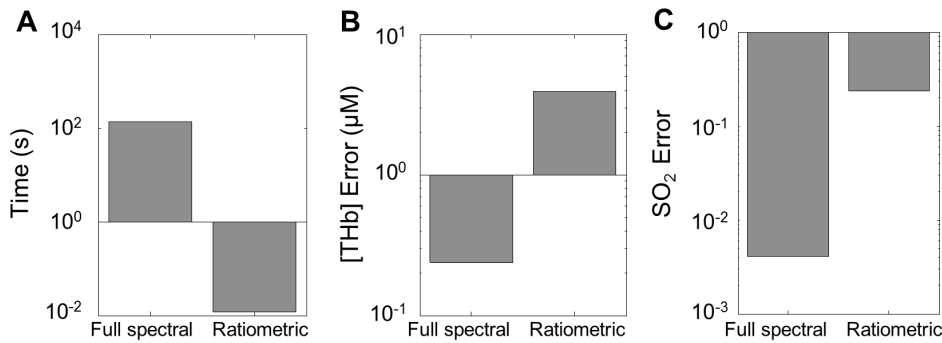


**Figure 6. Comparison between the scalable inverse MC analysis and the ratiometric analysis.** (A) Elapsed time of extracting 100 MC simulated phantoms for the scalable inverse MC model and the ratiometric analysis. (B) Absolute [THb] error and (C) SO<sub>2</sub> errors for MC and ratiometric analysis.

doi:10.1371/journal.pone.0082977.g006

Figure 10A was built based on the SO<sub>2</sub> and the log([THb]) and the full spectral MC ROC curve in Figure 10B was built based on SO<sub>2</sub>, log([THb]) and log(μ<sub>s</sub>). Both ratiometric ROC curves in Figure 10A and 10B were built based on SO<sub>2</sub> and log([THb]).

## Discussion

A simple and fast analysis for quantitative extraction of [THb] and SO<sub>2</sub> of tissues is presented. The analysis used a look-up table that allows conversion of the ratio of the diffuse reflectance at two selected wavelengths into [THb] and SO<sub>2</sub> values. This ratiometric analysis uses two isosbestic wavelengths for the calculation of [THb] and one isosbestic wavelength along with a wavelength where a local maximum difference in the extinction coefficients of deoxy- and oxy- hemoglobin exists for SO<sub>2</sub>. A total of 10 wavelength-pairs were tested for extraction of the [THb] while 25 wavelength-pairs were tested for SO<sub>2</sub>. The wavelength-pairs with the least dependence on tissue scattering were selected through rigorous tests on a total of 24805 spectra. The look-up tables used to translate the reflectance ratio into quantitative values were built for specific experimental probe-geometries and theoretically can be extended to any given source-detector configuration. Further,

calibration using specific experimental phantoms ensured that the ratiometric analysis could directly be used on experimentally measured data. Once analytical equations for the ratiometric analysis were generated, extraction of [THb] and SO<sub>2</sub> values from experimentally measured diffuse reflectance was over 4000 times faster than the scalable inverse full spectral MC analysis with minimal loss in accuracy. Even though the ratiometric analysis is not expected to be as accurate as the inverse full spectral MC analysis, the ratiometric analysis achieves similar contrast between malignant and the benign tissues in three different organ sites for a wide range of tissue vascularity and for tissues with multiple absorbers.

A prominent hemoglobin absorption feature (Soret band) occurred around 410–420 nm in the visible spectrum. However, we omitted the absorption peaks of hemoglobin around the 410–420 nm since most silicon-based detectors have lower sensitivities in this region. In order to detect the hemoglobin absorption around 410–420 nm, higher power light sources or more sensitive detectors would be required. In order to leverage relatively low priced light sources, the wavelengths were chosen from 500 nm to 600 nm (visible spectrum) in this manuscript.

The purpose of the bandpass simulations was to understand if the best [THb] or the SO<sub>2</sub> ratios would change for the different systems used. Our results show that 584/545 and 539/545 are the best ratios for the simulated results with three different bandpass values. Both 584/545 and 539/545 can extract [THb] or SO<sub>2</sub> with low errors and both ratios have low sensitivity to scattering. Although different systems might have different bandpasses, the relative rankings of the [THb] ratios and SO<sub>2</sub> ratios for error and the sensitivity to scattering remain the same. The clinical data has three different bandpasses. The band passes were 1.5 nm and 1.9 nm for the head and neck and breast data, respectively. The bandpasses were 1.9 nm or 3.5 nm for the cervical data. The extracted data with the ratiometric analysis show good agreement with the full spectral MC extracted values. In addition, the simulated [THb] results in Figures 4A and 4B are consistent except that 570/545 has higher errors in the experimental data. We also believe the 74415 (24805 spectra \* 3 different bandpass values) MC-simulated spectra can account for a wide range of optical properties and thus, is more comprehensive than the experimental data.

The sensitivities of the ratiometric analysis to the scattering power were tested since the scattering power is likely to change in the real tissues. As can be seen in Figure 5, the accuracies varied as the scattering power has changed. Although the ratiometric analysis is less accurate when the scattering power varies than

**Table 4. Correlation coefficients and *p*-values between the ratiometric analysis and the Monte Carlo analysis.**

Study		[THb]		SO <sub>2</sub>	
		<i>r</i>	<i>p</i>	<i>r</i>	<i>p</i>
Cervix	All Tissues	0.69	<0.01	0.43	<0.01
	Normal	0.66	<0.01	0.34	0.02
	CIN1	0.62	0.01	0.5	0.05
	CIN2+	0.76	<0.01	0.46	0.13
Head and neck	All Tissues	0.92	<0.01	0.87	<0.01
	Glottic	0.97	<0.01	0.91	<0.01
	Lymphoid	0.72	<0.01	0.85	<0.01
	Mucosal	0.92	<0.01	0.87	<0.01
Breast	All Tissues	0.77	<0.01	0.71	<0.01
	Tumor	0.85	<0.01	0.63	<0.01
	Benign	0.71	<0.01	0.56	<0.01
	Adipose	0.82	<0.01	0.48	<0.01

doi:10.1371/journal.pone.0082977.t004

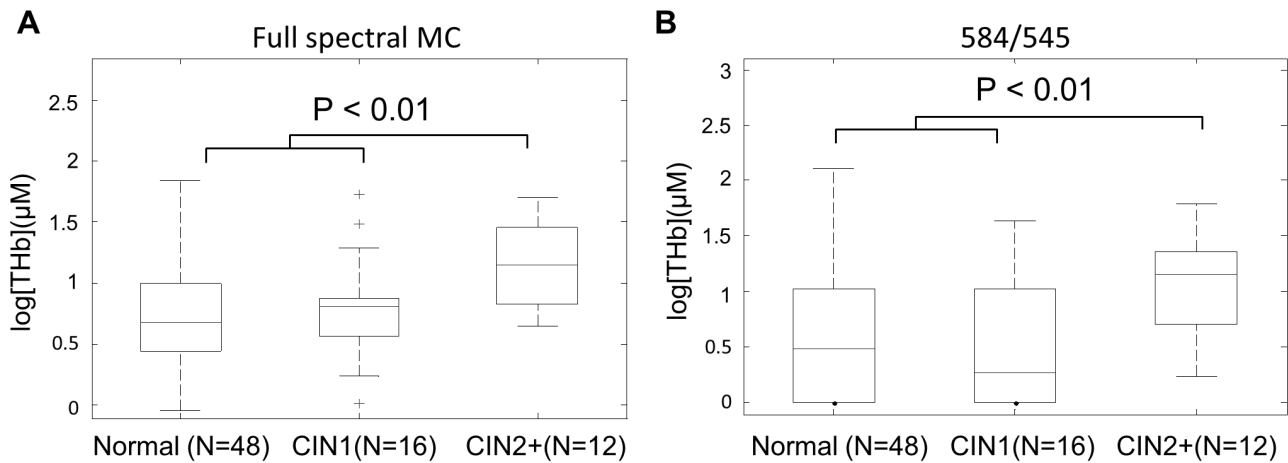


**Figure 7. Results for the *in vivo* cervix study.** Boxplots for (A) full spectral Monte Carlo extracted and (B) ratiometrically (584/545) extracted [THb]. Unpaired two-sided student *t*-tests were performed between normal, CIN1, and CIN2+. Significant *p*-values are shown. doi:10.1371/journal.pone.0082977.g007

when the scattering power is a constant, the contrast between malignant and non-malignant tissues in breast and head and neck or the contrast between the low-grade and the high-grade cervical tissues is still preserved. In addition, our analysis found a high degree of correlation in the extracted [THb] and SO<sub>2</sub> values between the ratiometric analysis and the inverse full spectral MC analysis. These correlations were especially high for measurements in head and neck tissues. Correlations between the extracted [THb] and SO<sub>2</sub> in cervical tissues were the lowest, relative to head and neck or breast tissues. These effects might be due to the fact that the [THb] was typically much higher in the head and neck and breast studies, relative to the cervical study (the averaged full spectral MC extracted [THb] for head and neck, breast and cervical tissues were, 57.8 μM, 14.2 μM and 5.9 μM respectively). In other words, correlations between the ratiometrically and the full spectral MC extracted [THb] or SO<sub>2</sub> are positively correlated to the full spectral MC extracted [THb]. This can be seen in Figure 11, which shows the scatter plot for the average MC extracted [THb] for the 9 tissue groups in Table 4 versus the correlation coefficients between the full spectral MC extracted and

ratiometrically-extracted [THb] and SO<sub>2</sub>. Because hemoglobin has very high extinction coefficients in the UV spectral-range relative to the visible, using wavelengths in the UV range could provide increased dynamic-range for sensing hemoglobin. This reasoning supports our previously published study [41], where the ratiometric technique for extraction of [THb] was superior for the 545/390, 452/390 and 529/390 ratios, relative to the 584/545 wavelength pair used here.

Although the ratiometric analysis was developed by assuming that hemoglobin was the primary absorber in tissue, the experimental measurements on human tissue can be influenced by absorbers other than hemoglobin [49] [50]. However, SO<sub>2</sub> and [THb] are the hallmarks of carcinogenesis and represent the features of a growing tumor. This has been published on widely and is useful in diagnostics and therapeutics [51] [52] [53] [54] [55]. For example, neovascularization increases with the development of cancer, and tumor hypoxia occurs as tumors outstrip their blood supply. Thus, being able to measure these endpoints with an optical technology that is optimized for speed and cost will have applications in early detection, diagnostics and response to

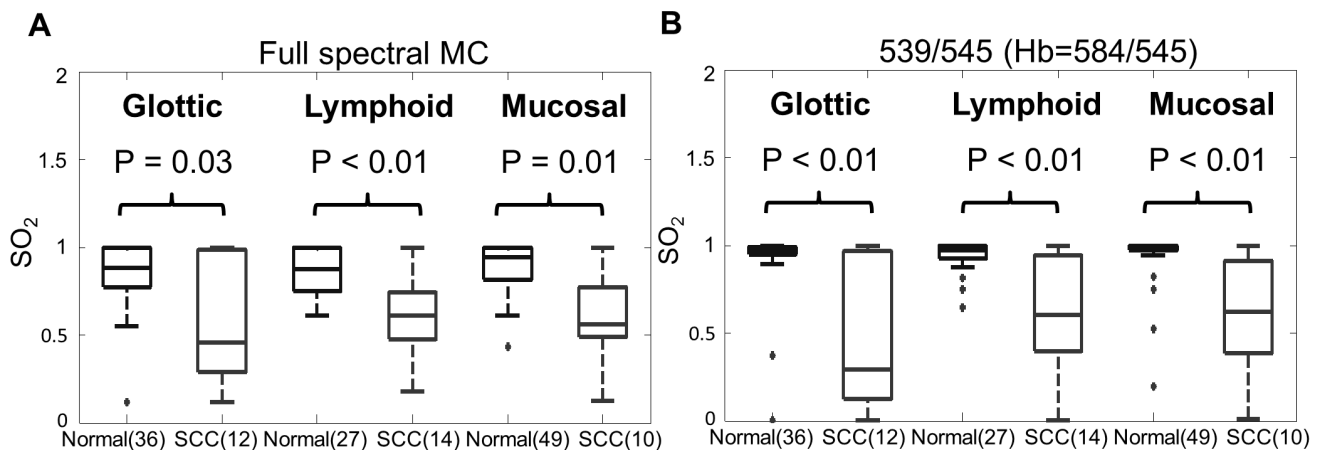


**Figure 8: Results for the *in vivo* head and neck study.** Boxplots for SO<sub>2</sub> at malignant and normal sites extracted with the (A) full spectral Monte Carlo analysis and the (B) ratiometric analysis. Wilcoxon rank-sum tests were performed between normal and SCC sites for each tissue type. Significant *p*-values from are shown. (SCC: squamous cell carcinoma). doi:10.1371/journal.pone.0082977.g008

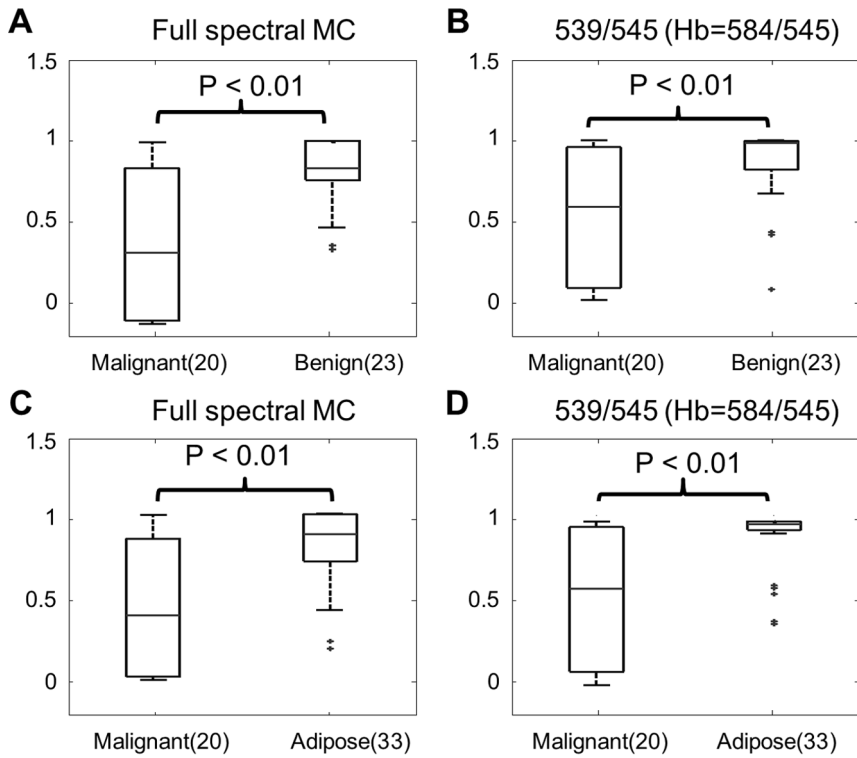


**Figure 9. Results for the *in vivo* breast study.** Boxplots for  $SO_2$  of the malignant and benign samples extracted with the (A) full spectral Monte Carlo analysis and (B) the ratiometric analysis. Boxplots for  $SO_2$  of the tumor and adipose samples extracted with the (C) full spectral Monte Carlo analysis and (D) the ratiometric analysis. Ratiometric [THb] was estimated with 584/545, and  $SO_2$  was estimated with 539/545. Wilcoxon rank-sum tests were performed for each group, and the significant  $p$ -values are shown. doi:10.1371/journal.pone.0082977.g009

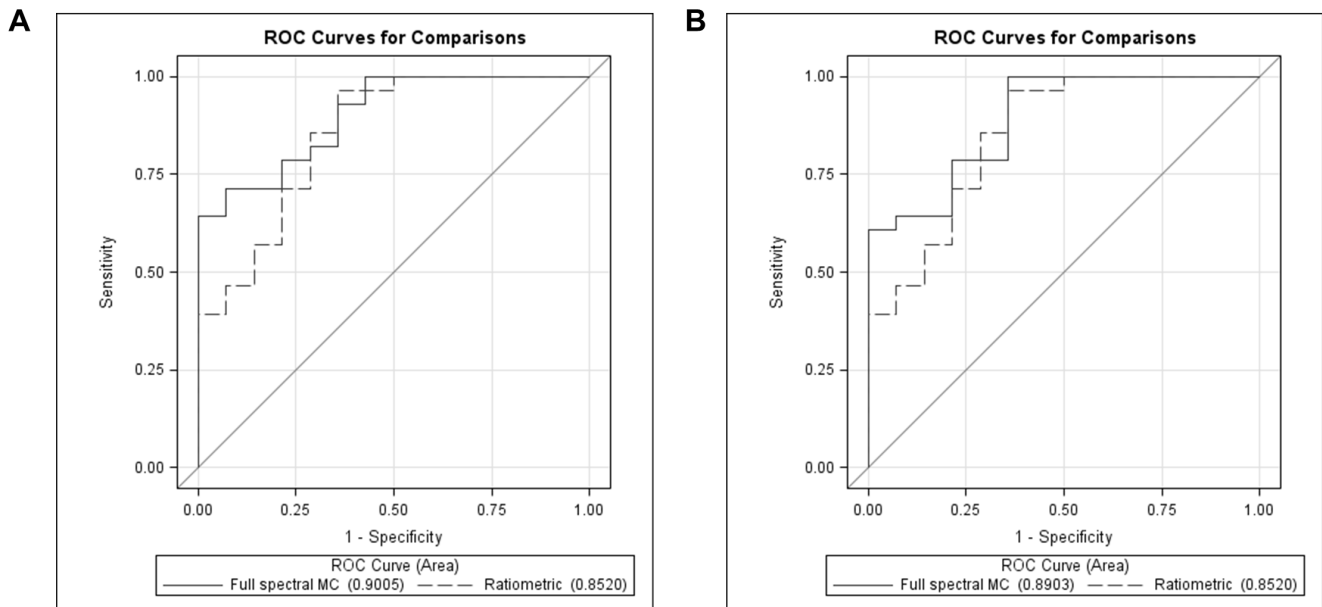


**Figure 10. The area under the receiver operating curves computed from the logistic regression model built base on different optical biomarkers from the full spectral MC and the ratiometric analyses for lymphoid tissues.** (A) Full spectral MC and the ratiometrically extracted  $SO_2$ ,  $\log([THb])$  were used for building the MC and the ratiometric logistic regression models respectively. (B)  $SO_2$ ,  $\log([THb])$ ,  $\log(\mu_s')$  were used to build the logistic regression model for the full spectral MC analysis and the ratiometric ROC curve was built based on the  $SO_2$ ,  $\log([THb])$ . doi:10.1371/journal.pone.0082977.g010

**Table 5.** The area under the receiver operating curves computed from the logistic regression model built base on different optical biomarkers from the full spectral MC and the ratiometric analyses.

<b>Breast</b>				
Full spectral MC optical biomarkers	AUC	Ratiometric optical biomarkers	AUC	p value
SO <sub>2</sub> , log([THb])	0.83	SO <sub>2</sub> , log([THb])	0.79	0.42
SO <sub>2</sub> , log([THb]), log(μ <sub>s</sub> ')	0.85	SO <sub>2</sub> , log([THb])	0.79	0.26
SO <sub>2</sub> , log([THb]), log(μ <sub>s</sub> '), log(β-carotene)	0.85	SO <sub>2</sub> , log([THb])	0.79	0.24
<b>Cervix</b>				
SO <sub>2</sub> , log([THb])	0.76	SO <sub>2</sub> , log([THb])	0.72	0.51
SO <sub>2</sub> , log([THb]), log(μ <sub>s</sub> ')	0.77	SO <sub>2</sub> , log([THb])	0.72	0.54
<b>Head and neck (Glottic)</b>				
SO <sub>2</sub> , log([THb])	0.79	SO <sub>2</sub> , log([THb])	0.76	0.69
SO <sub>2</sub> , log([THb]), log(μ <sub>s</sub> ')	0.83	SO <sub>2</sub> , log([THb])	0.76	0.48
<b>Head and neck (Lymphoid)</b>				
SO <sub>2</sub> , log([THb])	0.90	SO <sub>2</sub> , log([THb])	0.85	0.32
SO <sub>2</sub> , log([THb]), log(μ <sub>s</sub> ')	0.89	SO <sub>2</sub> , log([THb])	0.85	0.40
<b>Head and neck (Mucosal)</b>				
SO <sub>2</sub> , log([THb])	0.81	SO <sub>2</sub> , log([THb])	0.86	0.13
SO <sub>2</sub> , log([THb]), log(μ <sub>s</sub> ')	0.83	SO <sub>2</sub> , log([THb])	0.86	0.31

doi:10.1371/journal.pone.0082977.t005

therapy. Although some tissues may have multiple absorbers in addition to Hb, the classification performances were not significantly affected when using only [THb] and SO<sub>2</sub> as parameters (in cervix and head & neck only). Further, optical technologies have a significant potential to have an impact in global health. The ratiometric analysis still worked reasonably well in breast tissue, where beta-carotene is a known absorber in the wavelength range used. The presence of beta-carotene could be one reason why we

obtained a slightly lower correlation coefficients between the ratiometric and full spectral MC analysis in the breast study, relative to the head and neck study. Overall, in all of the clinical studies, the [THb] extracted from the ratiometric analysis were better correlated to full spectral MC values, in comparison to the SO<sub>2</sub> values. The effect of beta-carotene is more obvious in the SO<sub>2</sub> estimation than in the [THb] estimation. This could possibly be due to the absorption of beta-carotene being 8.5 times lower in the

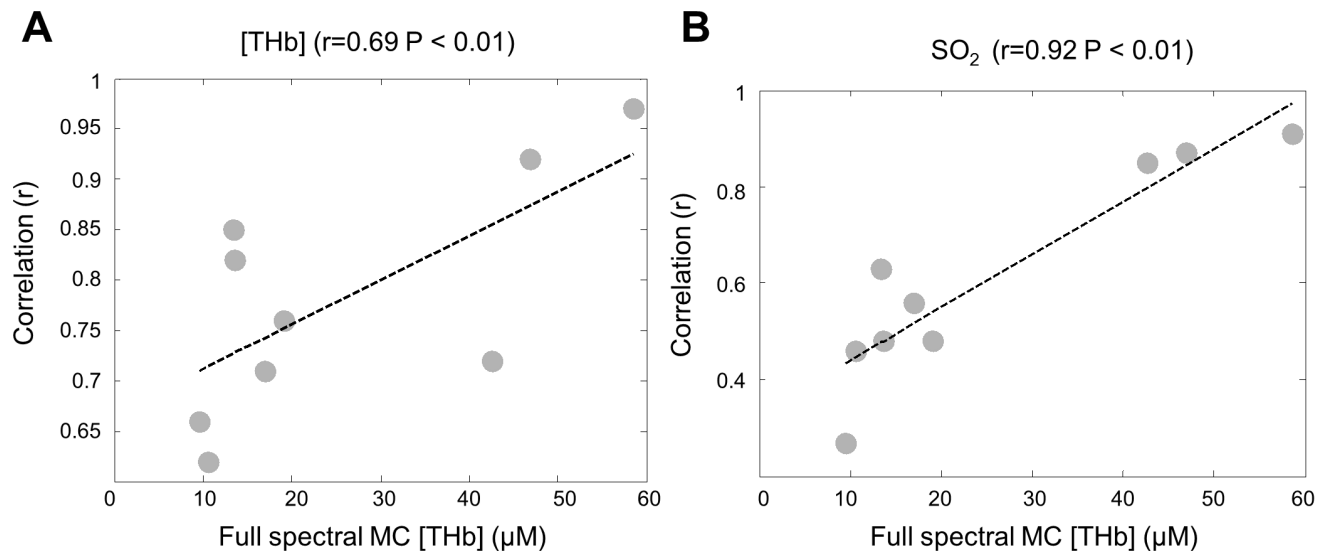


**Figure 11. Correlation between Monte Carlo analysis and ratiometric analysis.** (A) Correlation coefficients between the full spectral Monte Carlo and ratiometrically extracted [THb] as a function of the average full spectral Monte Carlo extracted [THb] for the 9 tissue groups in Table 4. (B) Correlation coefficients between the full spectral Monte Carlo and ratiometrically extracted SO<sub>2</sub> as a function of the average full spectral Monte Carlo extracted [THb] for the 9 tissue groups in Table 4. doi:10.1371/journal.pone.0082977.g011

550–600 nm compared to 500–550 nm. However, despite the lower correlation for the  $\text{SO}_2$  estimation in the breast tissues, the ratiometric analysis is still able to preserve the contrast between the malignant and non-malignant breast tissues observed with the results using the full spectral MC analysis.

In this manuscript, we have specifically shown the potential utility of the ratiometric analysis for diffuse reflectance imaging. Since our ratiometric analysis only involves wavelengths at 539, 545 and 584 nm, this analysis can be incorporated into any system with the use of a simple white LED and appropriate bandpass filters. With appropriate optimization for wavelength and illumination and collection geometries, the ratiometric analysis might be applied to a variety of spectral imaging systems [56] [57] [58] [59]. For example, this analysis can be incorporated into previously developed fiber-less technology [59], where a Xenon lamp and light filters are used to illuminate the tissue at different wavelengths of light. The illumination light was delivered through free space with a quartz light delivery tube. A custom photodiode array is in contact with the tissue to directly measure diffuse reflectance from a large area of tissue. With proper modifications of this system and combined with the ratiometric analysis, real-time [THb] and  $\text{SO}_2$  imaging is possible.

## References

- Kujan O, Glennly AM, Oliver RJ, Thakker N, Sloan P (2006) Screening programmes for the early detection and prevention of oral cancer. *Cochrane Database Syst Rev* 3: CD004150.
- Sankaranarayanan R, Ramadas K, Thomas G, Muwonge R, Thara S, et al. (2005) Effect of screening on oral cancer mortality in Kerala, India: a cluster-randomised controlled trial. *Lancet* 365: 1927–1933.
- (2007) Early detection is the key to beating oral cancer, *Oral Cancer News*. Oral Cancer Foundation.
- CDC (2009) Oral Cancer Background Papers. Accessed: 2009 Sept. 23.
- Adams EK, Breen N, Joski PJ (2007) Impact of the National Breast and Cervical Cancer Early Detection Program on mammography and Pap test utilization among white, Hispanic, and African American women: 1996–2000. *Cancer* 109: 348–358.
- Saslow D, Runowicz CD, Solomon D, Moscicki AB, Smith RA, et al. (2003) American Cancer Society Guideline for the Early Detection of Cervical Neoplasia and Cancer. *J Low Genit Tract Dis* 7: 67–86.
- Lawson HW, Henson R, Bobo JK, Kaeser MK (2000) Implementing recommendations for the early detection of breast and cervical cancer among low-income women. *MMWR Recomm Rep* 49: 37–55.
- Sherris J, Herdman C, Elias C (2001) Cervical cancer in the developing world. *West J Med* 175: 231–233.
- Skala MC, Palmer GM, Vrotsos KM, Gendron-Fitzpatrick A, Ramanujam N (2007) Comparison of a physical model and principal component analysis for the diagnosis of epithelial neoplasias in vivo using diffuse reflectance spectroscopy. *Opt Express* 15: 7863–7875.
- Chang VT, Cartwright PS, Bean SM, Palmer GM, Bentley RC, et al. (2009) Quantitative physiology of the precancerous cervix in vivo through optical spectroscopy. *Neoplasia* 11: 325–332.
- Muller MG, Valdez TA, Georgakoudi I, Backman V, Fuentes C, et al. (2003) Spectroscopic detection and evaluation of morphologic and biochemical changes in early human oral carcinoma. *Cancer* 97: 1681–1692.
- de Veld DC, Skurichina M, Witjes MJ, Duin RP, Sterenberg HJ, et al. (2005) Autofluorescence and diffuse reflectance spectroscopy for oral oncology. *Lasers Surg Med* 36: 356–364.
- Sharwani A, Jerjes W, Salih V, Swinson B, Bigio IJ, et al. (2006) Assessment of oral premalignancy using elastic scattering spectroscopy. *Oral Oncol* 42: 343–349.
- Subhash N, Mallia JR, Thomas SS, Mathews A, Sebastian P, et al. (2006) Oral cancer detection using diffuse reflectance spectral ratio R540/R575 of oxygenated hemoglobin bands. *J Biomed Opt* 11: 014018.
- Amelink A, Kaspers OP, Sterenberg HJ, van der Wal JE, Roodenburg JL, et al. (2008) Non-invasive measurement of the morphology and physiology of oral mucosa by use of optical spectroscopy. *Oral Oncol* 44: 65–71.
- Rahman M, Chaturvedi P, Gillenwater AM, Richards-Kortum R (2008) Low-cost, multimodal, portable screening system for early detection of oral cancer. *J Biomed Opt* 13: 030502.
- Schwarz RA, Gao W, Daye D, Williams MD, Richards-Kortum R, et al. (2008) Autofluorescence and diffuse reflectance spectroscopy of oral epithelial tissue using a depth-sensitive fiber-optic probe. *Appl Opt* 47: 825–834.

## Conclusion

A rapid analytical ratiometric analysis for determining [THb] and  $\text{SO}_2$  in head and neck, cervical, and breast tissues was presented. This analysis is non-invasive, label-free, quantitative, and fast. The ratiometric analysis requires the diffuse reflectance only from three selected wavelengths to calculate both [THb] and  $\text{SO}_2$ . Thus, the system design could be simple, portable, and potentially useful for global health applications. The fast computation speed allows near real-time [THb] and  $\text{SO}_2$  mapping of tissue. This will provide important physiological information for many clinical applications, from cancer screening to diagnostics to treatment.

## Acknowledgments

The authors would like to thank Drs. Stephanie Kennedy, Torre Bydlon, Narasimhan Rajaram, J. Quincy Brown, and Vivide Chang for their contributions to this project.

## Author Contributions

Conceived and designed the experiments: FH KV NR. Performed the experiments: FH. Analyzed the data: FH. Contributed reagents/materials/analysis tools: FH KV AE. Wrote the paper: FH KV JL AE CM WL NR.

- Mirabal YN, Chang SK, Atkinson EN, Malpica A, Follen M, et al. (2002) Reflectance spectroscopy for in vivo detection of cervical precancer. *J Biomed Opt* 7: 587–594.
- Chang SK, Mirabal YN, Atkinson EN, Cox D, Malpica A, et al. (2005) Combined reflectance and fluorescence spectroscopy for in vivo detection of cervical pre-cancer. *J Biomed Opt* 10: 024031.
- Follen M, Crain S, MacAulay C, Basen-Engquist K, Cantor SB, et al. (2005) Optical technologies for cervical neoplasia: update of an NCI program project grant. *Clin Adv Hematol Oncol* 3: 41–53.
- Marin NM, Milbourne A, Rhodes H, Ehlen T, Miller D, et al. (2005) Diffuse reflectance patterns in cervical spectroscopy. *Gynecol Oncol* 99: S116–120.
- Arifler D, MacAulay C, Follen M, Richards-Kortum R (2006) Spatially resolved reflectance spectroscopy for diagnosis of cervical precancer: Monte Carlo modeling and comparison to clinical measurements. *J Biomed Opt* 11: 064027.
- Cardenas-Turanzas M, Freeberg JA, Benedet JL, Atkinson EN, Cox DD, et al. (2007) The clinical effectiveness of optical spectroscopy for the in vivo diagnosis of cervical intraepithelial neoplasia: where are we? *Gynecol Oncol* 107: S138–146.
- Freeberg JA, Benedet JL, MacAulay C, West LA, Follen M (2007) The performance of fluorescence and reflectance spectroscopy for the in vivo diagnosis of cervical neoplasia; point probe versus multispectral approaches. *Gynecol Oncol* 107: S248–255.
- Wang A, Nammalavar V, Drezek R (2007) Targeting spectral signatures of progressively dysplastic stratified epithelia using angularly variable fiber geometry in reflectance Monte Carlo simulations. *J Biomed Opt* 12: 044012.
- Arifler D, Schwarz RA, Chang SK, Richards-Kortum R (2005) Reflectance spectroscopy for diagnosis of epithelial precancer: model-based analysis of fiber-optic probe designs to resolve spectral information from epithelium and stroma. *Appl Opt* 44: 4291–4305.
- Lane PM, Gilhuly T, Whitehead P, Zeng H, Poh CF, et al. (2006) Simple device for the direct visualization of oral-cavity tissue fluorescence. *J Biomed Opt* 11: 024006.
- Pavlova I, Weber CR, Schwarz RA, Williams MD, Gillenwater AM, et al. (2009) Fluorescence spectroscopy of oral tissue: Monte Carlo modeling with site-specific tissue properties. *J Biomed Opt* 14: 014009.
- Hasina R, Lingen MW (2001) Angiogenesis in oral cancer. *J Dent Educ* 65: 1282–1290.
- Georgakoudi I, Sheets EE, Muller MG, Backman V, Crum CP, et al. (2002) Trimodal spectroscopy for the detection and characterization of cervical precancers in vivo. *Am J Obstet Gynecol* 186: 374–382.
- Liu Q, Ramanujam N (2006) Sequential estimation of optical properties of a two-layered epithelial tissue model from depth-resolved ultraviolet-visible diffuse reflectance spectra. *Appl Opt* 45: 4776–4790.
- Zhu C, Palmer GM, Breslin TM, Xu F, Ramanujam N (2005) Use of a multiseparation fiber optic probe for the optical diagnosis of breast cancer. *J Biomed Opt* 10: 024032.
- Palmer GM, Ramanujam N (2006) Monte Carlo-based inverse model for calculating tissue optical properties. Part I: Theory and validation on synthetic phantoms. *Appl Opt* 45: 1062–1071.

34. Beumer HW, Vishwanath K, Puscas L, Afshari HR, Ramanujam N, et al. (2011) Detection of Squamous Cell Carcinoma and Corresponding Biomarkers Using Optical Spectroscopy. *Otolaryngology-Head and Neck Surgery* 144: 390–394.
35. PATH Cervical cancer prevention initiatives at PATH. PATH.
36. Goldie SJ, Gaffikin L, Goldhaber-Fiebert JD, Gordillo-Tobar A, Levin C, et al. (2005) Cost-Effectiveness of Cervical-Cancer Screening in Five Developing Countries. *N Engl J Med* 353: 2158–2168.
37. Sankaranarayanan R, Nene B, Shastri S, Jayant K, Muwonge R, et al. (2009) HPV screening for cervical cancer in rural India. *The New England Journal of Medicine* 360: 1385.
38. Zeferino LC, Derchain SF (2006) Cervical cancer in the developing world. *Best Practice & Research Clinical Obstetrics & Gynaecology* 20: 339–354.
39. Ellsworth ML, Pittman RN, Ellis CG (1987) Measurement of Hemoglobin Oxygen-Saturation in Capillaries. *American Journal of Physiology* 252: H1031–H1040.
40. Pittman RN, Duling BR (1975) New Method for Measurement of Percent Oxyhemoglobin. *Journal of Applied Physiology* 38: 315–320.
41. Phelps JE, Vishwanath K, Chang VTC, Ramanujam N (2010) Rapid ratiometric determination of hemoglobin concentration using UV-VIS diffuse reflectance at isosbestic wavelengths. *Optics Express* 18: 18779–18792.
42. Palmer GM, Ramanujam N (2006) Monte Carlo-based inverse model for calculating tissue optical properties. Part I: Theory and validation on synthetic phantoms. *Applied Optics* 45: 1062–1071.
43. Bender JE, Vishwanath K, Moore LK, Brown JQ, Chang V, et al. (2009) A Robust-Monte Carlo Model for the Extraction of Biological Absorption and Scattering In Vivo. *Ieee Transactions on Biomedical Engineering* 56: 960–968.
44. Chang VT, Bean SM, Cartwright PS, Ramanujam N (2010) Visible light optical spectroscopy is sensitive to neovascularization in the dysplastic cervix. *J Biomed Opt* 15: 057006.
45. Brown JQ, Wilke LG, Geradts J, Kennedy SA, Palmer GM, et al. (2009) Quantitative optical spectroscopy: a robust tool for direct measurement of breast cancer vascular oxygenation and total hemoglobin content in vivo. *Cancer Res* 69: 2919–2926.
46. Chang VTC, Cartwright PS, Bean SM, Palmer GM, Bentley RC, et al. (2009) Quantitative Physiology of the Precancerous Cervix In Vivo through Optical Spectroscopy. *Neoplasia* 11: 325–332.
47. Vishwanath K, Chang K, Klein D, Deng YF, Chang V, et al. (2011) Portable, Fiber-Based, Diffuse Reflection Spectroscopy (DRS) Systems for Estimating Tissue Optical Properties. *Appl Spectrosc* 65: 206–215.
48. Delong ER, Delong DM, Clarkepearson DI (1988) Comparing the Areas under 2 or More Correlated Receiver Operating Characteristic Curves - a Nonparametric Approach. *Biometrics* 44: 837–845.
49. Anderson RR, Parrish JA (1981) The optics of human skin. *J Invest Dermatol* 77: 13–19.
50. Vangemert MJC, Jacques SL, Sterenberg HJCM, Star WM (1989) Skin Optics. *Ieee Transactions on Biomedical Engineering* 36: 1146–1154.
51. Nordmark M, Bentzen SM, Rudat V, Brizel D, Lartigau E, et al. (2005) Prognostic value of tumor oxygenation in 397 head and neck tumors after primary radiation therapy. An international multi-center study. *Radiotherapy and Oncology* 77: 18–24.
52. Brizel DM, Sibley GS, Prosnitz LR, Scher RL, Dewhirst MW (1997) Tumor hypoxia adversely affects the prognosis of carcinoma of the head and neck. *International Journal of Radiation Oncology Biology Physics* 38: 285–289.
53. Warde P, O'Sullivan B, Bristow RG, Panzarella T, Keane TJ, et al. (1998) T1/T2 glottic cancer managed by external beam radiotherapy: The influence of pretreatment hemoglobin on local control. *International Journal of Radiation Oncology Biology Physics* 41: 347–353.
54. Dubray B, Mosseri V, Brunin F, Jaulerry C, Poncet P, et al. (1996) Anemia is associated with lower local-regional control and survival after radiation therapy for head and neck cancer: A prospective study. *Radiology* 201: 553–558.
55. Lee WR, Berkey B, Marcial V, Fu KK, Cooper JS, et al. (1998) Anemia is associated with decreased survival and increased locoregional failure in patients with locally advanced head and neck carcinoma: A secondary analysis of RTOG 85–27. *International Journal of Radiation Oncology Biology Physics* 42: 1069–1075.
56. Cuccia DJ, Bevilacqua F, Durkin AJ, Ayers FR, Tromberg BJ (2009) Quantitation and mapping of tissue optical properties using modulated imaging. *J Biomed Opt* 14.
57. Gao L, Kester RT, Tkaczyk TS (2009) Compact Image Slicing Spectrometer (ISS) for hyperspectral fluorescence microscopy. *Optics Express* 17: 12293–12308.
58. Wagadarikar AA, Pitsianis NP, Sun XB, Brady DJ (2009) Video rate spectral imaging using a coded aperture snapshot spectral imager. *Optics Express* 17: 6368–6388.
59. Dhar S, Lo JY, Palmer GM, Brooke MA, Nichols BS, et al. (2012) A diffuse reflectance spectral imaging system for tumor margin assessment using custom annular photodiode arrays. *Biomed Opt Express* 3: 3211–3222.